Fatigue Crack Growth Monitoring and Investigation on G20Mn5QT Cast Steel and Welds via Acoustic Emission

(Article begins on next page)

22 November 2024

Article

Fatigue Crack Growth Monitoring and Investigation on G20Mn5QT Cast Steel and Welds via Acoustic Emission

Qingyang Liu [1], Zhenli Zhang [1], Giuseppe Lacidogna [2], Yantao Xu [3] and Jie Xu [3,*]

[1] Shandong Electric Power Engineering Consulting Institute Corp., Ltd., Jinan 250013, China
[2] Department of Structural, Geotechnical and Building Engineering, Politecnico di Torino, 10129 Turin, Italy
[3] School of Civil Engineering, Tianjin University, Tianjin 300072, China
[*] Correspondence: jxu@tju.edu.cn

Abstract: The fatigue crack growth properties of G20Mn5QT cast steel and corresponding butt welds, using compact tension specimens, were monitored and investigated via acoustic emission (AE) techniques. Fatigue crack growth is a combination of cyclic plastic deformations before the crack tip, tensile crack fractures, and shear crack fractures. The cyclic plastic deformations release the maximum amount of energy, which accounts for half of the total energy, and the second-largest number of AE signals, which are of the continuous-wave type. The tensile crack fractures release the second-largest amount of energy and the largest number of AE signals, which are of the burst-wave type. The shear crack fractures release the least amount of energy and the lowest number of AE signals, which are similar to the burst type, albeit with a relatively longer rise time and duration. Crack tip advancement can be regarded as a discontinuous process. The critical area before the crack tip brittlely ruptures when the fatigue damage caused by cyclic plastic deformations reaches critical status. The ruptures produce a large number of tensile crack fractures and rare shear crack fractures. Through fractography observation, the shear crack fractures occur probabilistically around defects caused by casting or welding, which lead to stress and strain in the local complex.

Keywords: fatigue crack growth; G20Mn5QT; butt welds; monitoring and investigation; acoustic emission

1. Introduction

G20Mn5QT cast steel is a type of low-carbon alloy steel specified in the European code EN 10293 [1]. With sufficient weldability, the static bearing performance of G20Mn5QT is quite similar to that of A572 (used in America), S335 (used in Europe), and Q345D (used in China). The mechanical properties of G20Mn5QT and related welds under different working conditions have been widely studied, such as adhesively bonded steel tubes [2], stress analysis of the fatigue behaviors of the girth butt weld within welded cast steel joints [3], and the environment effects of G20Mn5QT cast steel [4–6]. Meanwhile, G20Mn5QT is usually cast into complex geometrical components, and under cyclic loads such as waves and winds, such load-bearing members and related welds can incur fatigue damage. Unfortunately, the fatigue resistance performance of G20Mn5QT and the corresponding butt welds is unsatisfactory [7,8]; the reasons for this may include the large stress concentrations and defects introduced during the casting and welding processes.

Recently, some investigations have been performed to reveal the characteristics of G20Mn5QT under cyclic loads. The strain–life curves of G20Mn5QT and related welds with Q345D were obtained by using uniaxial smooth bar specimens, and the Manson–Coffin model was proposed to evaluate the fatigue life [8]. Lu et al. analyzed the influence of corrosion on the fatigue properties of G20Mn5QT cast steel and Q355 steel butt welds in 3.5-wt% NaCL solution and undergoing a dry–wet cycle [9,10]. Han et al. investigated the fatigue performance and fatigue life prediction method of G20Mn5QT cast steel

notches [11]. However, no research discussing the mechanisms of fatigue crack growth in G20Mn5QT and the corresponding welds has been reported.

Acoustic emission (AE) technology is an effective method of non-destructive monitoring to evaluate material damage [12–14]. AE sensors collect stress waves generated due to the rapid energy release during the deformation of fracture sources and transform them into electrical signals. By analyzing the AE signals, information regarding the mechanism of the AE source can be obtained.

Several studies have attempted to investigate the AE characteristics during the fatigue crack growth process in metal materials. The AE signals exhibited different responses in different fatigue crack growth stages [15–17], and the cracks' stable growth stage can be further divided into two sub-stages based on AE activity [18,19]. Meanwhile, the welds demonstrated greater AE activity and more complex mechanism of AE sources compared to those of the base metal [17,20–22]. It was found that both the AE hit release rate and AE energy release rate exhibited positive correlations with fatigue crack growth rates [23–25]; this phenomenon could be employed to predict fatigue residual life. Considering the irregularity of AE behaviors, an artificial neural network [26,27] has been introduced into the fatigue crack growth estimation process to improve the accuracy. Moreover, AE could also be used in structural health monitoring. For example, Megid et al. [28] monitored fatigue cracks on the eye-bars of the Alexandra bridge, which is a 587 m long steel truss bridge located on the boundary between Ottawa and Gatineau, Canada. The results showed that AE is a very reliable technology for confirming or denying fatigue cracks initiation and assessing the condition of existing cracks, and it is a cost-effective component in structural health monitoring. In addition, lots of scholars have employed AE to monitor structure damage and fatigue cracks in pressure vessels [29], cables and chains [30], tower structures [31], rail tracks [32], and welded joints [21]. AE monitoring technology has not only been found applicable for metal materials such as aluminium alloy (the PLC effect) [25], titanium alloy [33], steel, and related welds [17] but also for concrete [34] and composite materials [35].

To reveal the damage mechanism of fatigue crack growth, cluster analysis is introduced. Cluster analysis is a mathematical algorithm that divides a dataset into several clusters according to the similarity of features. This method is quite suitable for the AE analysis of structures that exhibit different modes of failure, partitioning the AE signals into clusters that correspond to the related damage mechanisms. Cluster analysis has been effectively applied to damage pattern recognition in anisotropic materials [36,37]. For damage pattern recognition in fatigue crack growth in metals, studies have indicated that the cluster algorithm can identify different damage modes and evaluate the stress–strain status at the crack tip [38,39].

Therefore, to fill in the research gaps concerning the AE behaviors of G20Mn5QT cast steel and related butt welds during fatigue crack growth, AE signals generated during fatigue crack growth tests employing compact tensile (CT) specimens were collected and investigated. Moreover, to distinguish AE sources, the AE signals were first classified into different clusters via the K-means clustering algorithm, and next, the time–frequency characteristics in each cluster were analyzed and compared to the micrographs of fracture surfaces. By analyzing the performances of different clusters during the crack growth process, the relationship between the AE and the fatigue crack mechanism was established for both G20Mn5QT cast steel and the related butt welds.

2. Experimental Section

2.1. Materials and Specimens

A 20 mm thick welding plate consisting of G20Mn5QT and Q345D was employed in this study. The butt weld with V groove is fabricated via CO_2 gas arc welding. The filler material was an ER50-6 wire with a diameter of 1.2 mm. During the welding process, the pre-heating temperature was controlled to be 150 °C, the weld inter-pass temperature was

controlled to be 200–250 °C, and the post-heating temperature was controlled to be 250 °C for approximately two hours.

The chemical compositions of G20Mn5QT and the weld wire were determined and are given in Table 1. The microstructures of the G20Mn5QT cast steel and butt welds were observed via an optical microscope and are presented in Figure 1. G20Mn5QT cast steel, as a low alloy and low-carbon (LALC) cast steel, was found in its tempered sorbite form for the observation of clumpy and needle-like ferrite, as shown in Figure 1a. In addition, fine dispersed carbides were distributed discontinuously along the grain boundaries and in the grain interior. The microstructures of the weld zone could be categorized as a homogeneous ferrite–pearlite structure with Widmanstätten patterns involving coarse grains of the ferritic phase and a number of oxide inclusions, as shown in Figure 1b.
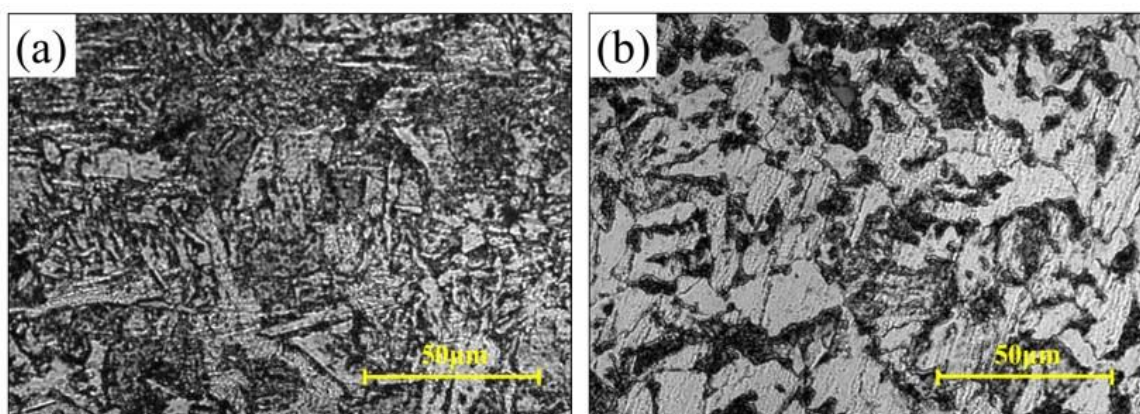

Figure 1. Microstructures: (**a**) G20Mn5QT cast steel; (**b**) welds.

All the compact tension (CT) specimens used in the tests were machined from the core material of the welding plate, as shown in Figure 2. The specimens used for testing the fatigue crack growth behaviors of G20Mn5QT were machined from an area far from the butt weld to avoid the influence of welding heat. For the specimens used for testing the fatigue crack growth behaviors of the butt weld, the pre-crack was ensured to be in the middle of the weld zone. The geometric specifications of the CT specimens, according to standard ASTM: E647 [40], are shown in Figure 3.
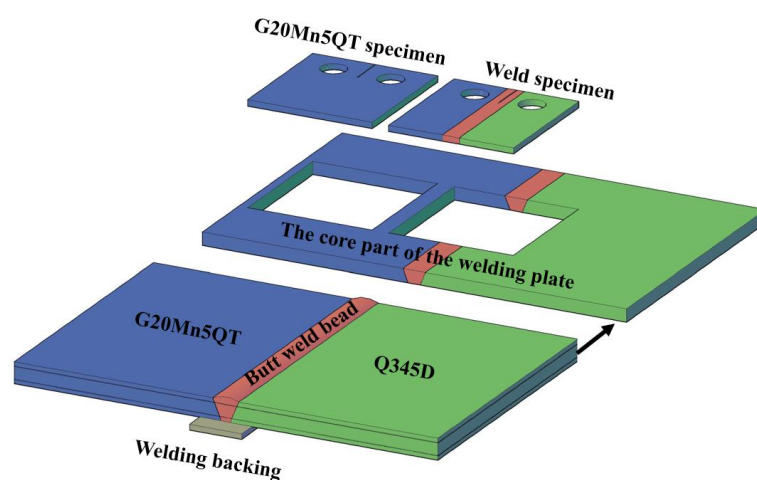

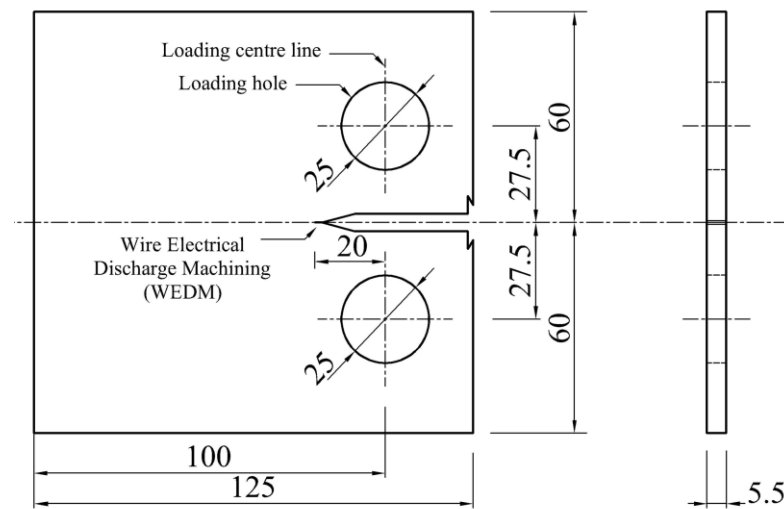**Figure 2.** Specimen machining zone.

Figure 3. Geometry of CT specimen.

Table 1. Chemical composition of G20Mn5QT base material and ER50-6 weld wire.

Material	C wt. %	Mn wt. %	Si wt. %	S wt. %	P wt. %	Ni wt. %	Fe wt. %
G20Mn5QT	0.190	1.340	0.400	0.008	0.014	0.600	Bal.
ER50-6	0.077	1.450	0.870	0.013	0.012	0.010	Bal.

2.2. Fatigue Crack Growth Tests

All the specimens were tested on an electrohydraulic servo fatigue testing machine under ambient temperature. The setup of the test is illustrated in Figure 4. The tests were carried out under sinusoidal cyclic loads with a maximum load of 18 kN and a load ratio of 0.5. In this test, the load frequency of 20 Hz was used to prefabricate the fatigue crack, and the load frequency of 4 Hz during the main phase of the fatigue test was applied to facilitate the precise observation of fatigue cracks. The stress intensity factor range ΔK could be calculated via Equation (1) [40].

$$\alpha = a / W$$

$$\Delta K = \frac{\Delta P}{B\sqrt{W}} \cdot \frac{(2+\alpha)}{(1-\alpha)^{3/2}} \left(0.886 + 4.64\alpha - 13.32\alpha^2 + 14.72\alpha^3 - 5.6\alpha^4\right), \tag{1}$$

where a is the crack length, which represents the distance between the fatigue crack tip and the loading centre line; W is the geometry parameter of the specimen (= 100 mm in this study); ΔK is the stress intensity factor range; ΔP is the load range; and B is the specimen thickness (= 5.5 mm in this study).

The fatigue crack length was measured using two different methods (see Figure 4). One was the visual measurement method, in which a high-magnification digital camera was employed, and a scale ruler was engraved on the surface of the specimen parallel to the crack. The test machine and the camera began operation simultaneously. The camera captured images of the crack tip every 4 min (960 load cycles). The crack length in the images was then measured. The other method was the compliance method. A COD extensometer was employed to measure the crack opening displacements every 400 load cycles, and the crack size was calculated based on Equation (2) [40].

$$\mu_{\mathrm{X}} = \left[\left(\frac{E v B}{P} \right)^{1/2} + 1 \right]^{-1} \tag{2}$$

$$a/W = 1.0010 - 4.6695\mu_{\mathrm{X}} + 18.460\mu_{\mathrm{X}}^{2} - 236.82\mu_{\mathrm{X}}^{3} + 1214.9\mu_{\mathrm{X}}^{4} - 2143.6\mu_{\mathrm{X}}^{5}$$

where E denotes the modulus of elasticity; v is the crack opening distance; B denotes the specimen thickness; and P is the load. The values measured using each method were compared and plotted in the same figure and subsequently fitted into a crack length–fatigue load cycle curve.

The fatigue crack growth tests were terminated at a crack length of 55 mm as at this point, the crack had already reached the unstable growth stage. After the fatigue crack growth tests, a scanning electron microscope (SEM) was employed to observe the fracture surfaces of all specimens.
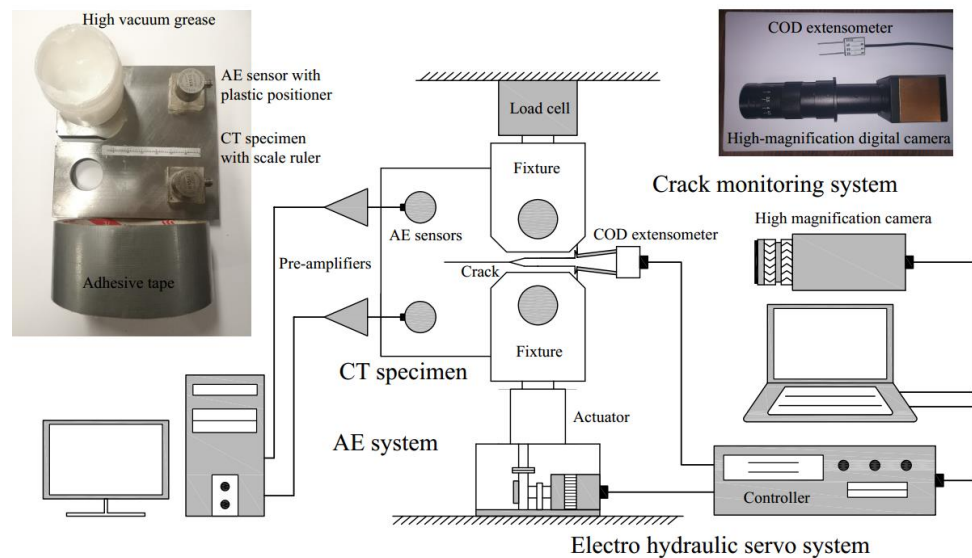

Figure 4. Test setup.

2.3. AE Setup

The AE signals generated during the fatigue crack growth tests were collected by a PC-based multi-channel monitoring system named SAMOS AE^win, manufactured by the Physical Acoustic Corporation (PAC). Two narrow-band piezoelectric ceramic transducers (R15*a*), having an operating frequency of 50 kHz to 200 kHz, were used to record the AE signals. To prevent the transducer from sliding or falling, first, a plastic positioner with a hole in the middle was bonded on the specimen. Next, the transducer was stuck in the hole and the detection surface and specimen surface were attached together by using an adhesive tape and high-vacuum grease (see Figure 4).

A preamplifier with a gain of 40 dB was used for each transducer. Before the fatigue crack growth tests were performed, a specimen without cracks was tested under the same load conditions and monitored to collect the external noises from the experimental setup. Based on this noise check test, the threshold was set as 36 dB to reduce the noise. Table 2 lists the main parameters of the AE system in the test. The AE parameter set was determined and verified using the pencil lead breaking test [41].

Table 2. Set of AE parameters.

| Transducer	R15α	Peak definite time	300 (μs)
Operating frequency	50–200 (kHz)	Hit definite time	600 (μs)
Preamplifier gain	40 (dB)	Hit lookout time	1000 (μs)
Threshold	36 (dB)	Hit length	4 (k)
Compatible filter	100–400 (kHz)	Sampling frequency	3 (MHz)

3. Results and Discussion

3.1. Fatigue Crack Growth and AE Activity

The fatigue crack growth rates of the G20Mn5QT and butt welds were compared. Figure 5 shows the relationship between the fatigue crack length and the fatigue load cycles. Figure 6 shows the relationship between the fatigue crack growth rate $\mathrm{d}a/\mathrm{d}N$ and the stress intensity factor range ΔK. It was noted that compared to the G20Mn5QT, the weld requires a larger number of load cycles to reach the same crack length. The fatigue crack growth rate of the weld is less than that of G20Mn5QT at low values of ΔK; however, the corresponding rates tend to be similar at high values of ΔK. The results obtained by fitting the fatigue crack growth rate curves according to the famous Paris law [42] (see Equation (3)) on double logarithmic coordinates can be represented as in Equation (4) ($R^2 = 0.97$) for G20Mn5QT and Equation (5) ($R^2 = 0.95$) for the weld.

$$\log_{10}(\mathrm{d}a/\mathrm{d}N) = m\log_{10}(\Delta K) + \log_{10}C \tag{3}$$

$$\log_{10}(\mathrm{d}a/\mathrm{d}N) = 3.07\log_{10}(\Delta K) - 8.34 \tag{4}$$

$$\log_{10}(\mathrm{d}a/\mathrm{d}N) = 3.78\log_{10}(\Delta K) - 9.52 \tag{5}$$
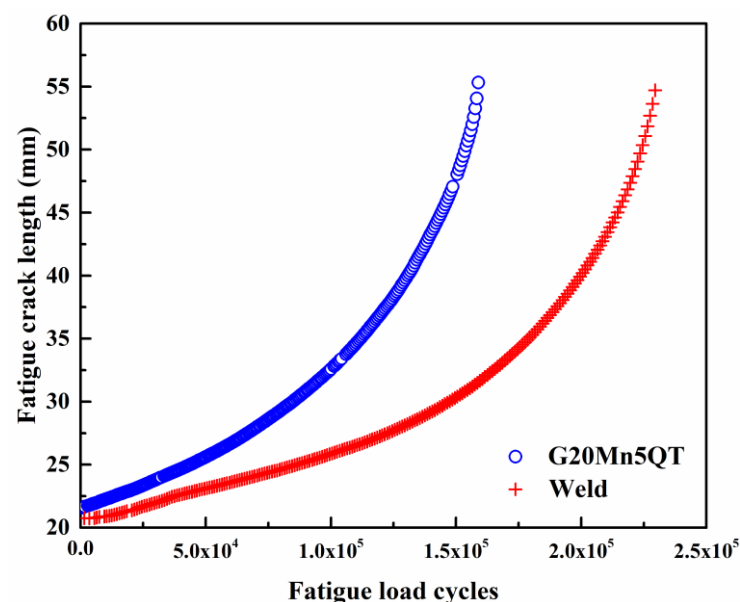
Figure 5. Fatigue crack length vs. load cycles.

According to the fatigue crack growth rate (FCGR) curves, the fatigue crack growth process can be divided into three stages, as shown in Figure 6. The transition from stage I to stage II pertains to crack initiation progressing to stable crack growth. The transition from stage II to stage III corresponds to the crack demonstrating unstable crack growth. The AE activities of G20Mn5QT and the weld vary considerably at different fatigue crack growth stages. The differences between ΔK, AE hit release rates, and energy release rates

for G20Mn5QT and the weld are shown in Figure 7. For G20Mn5QT, the hit and energy release rates reach the first peak at the end of stage I and later decline rapidly. For the weld, the hit and energy release rates also increase in stage I, but they reach the first peak at the boundary between stage I and stage II and decline gradually compared to the corresponding values for the case of G20Mn5QT at the beginning of stage II. In stage II, the AE activity remains stable and relatively low level at first; however, it resumes growth in the middle of stage II as the fatigue crack propagation approaches stage III. The regrowth point for G20Mn5QT appears earlier than it does for the weld. In stage III, the fatigue crack rapidly grows to the point of ultimate failure, and the hit and energy release rates become discrete and unstable.
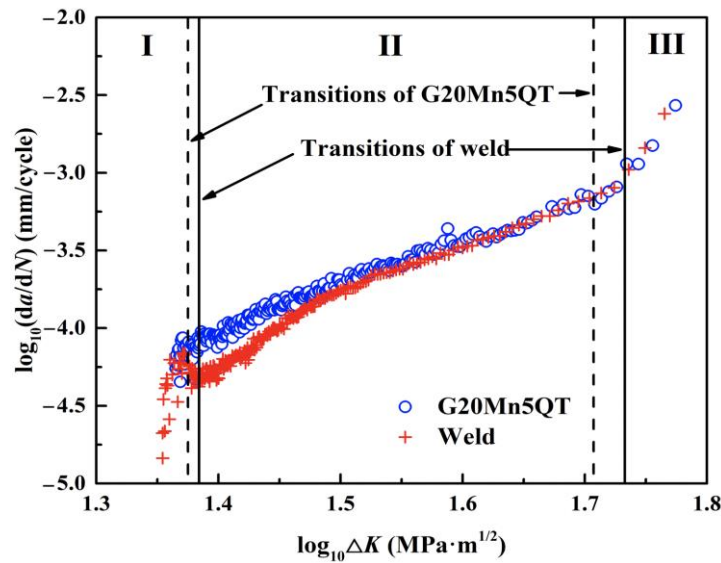

Figure 6. Fatigue crack growth rate vs. stress intensity factor range.

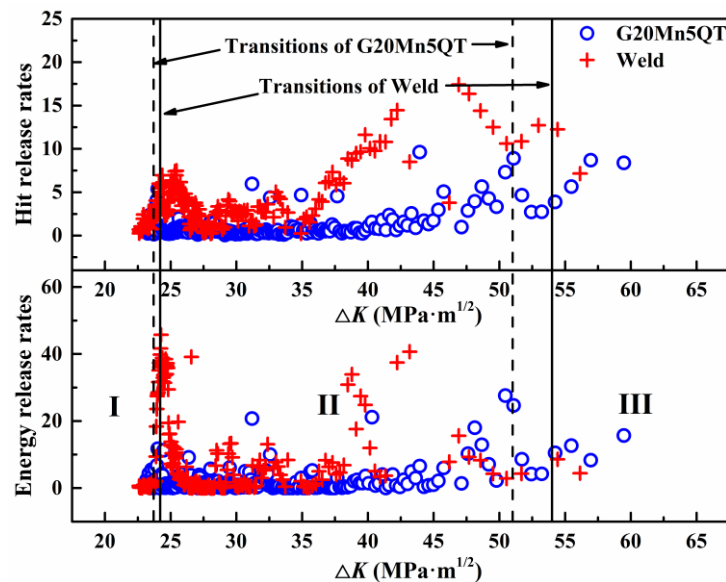**Figure 7.** AE hit and energy release rates.

Therefore, the cumulative hit and energy of G20Mn5QT demonstrate rapid accumulation in stage I and later demonstrate a stable increase in the first half of stage II. In contrast, the cumulative hit and energy of the weld indicate a high increase rate at the beginning of stage II, as shown in Figure 8. An obvious inflection point on the cumulative curve

of the weld in stage II can be observed, and it divides stage II into two sub-stages: IIa and IIb. However, the G20Mn5QT material does not demonstrate such a behavior involving sub-stages. Moreover, the AE activity of the weld is higher than that of G20Mn5QT when comparing the cumulative AE hit and energy, as shown in Figure 8. This phenomenon was also reported in some studies focusing on the base metal and weld [17].
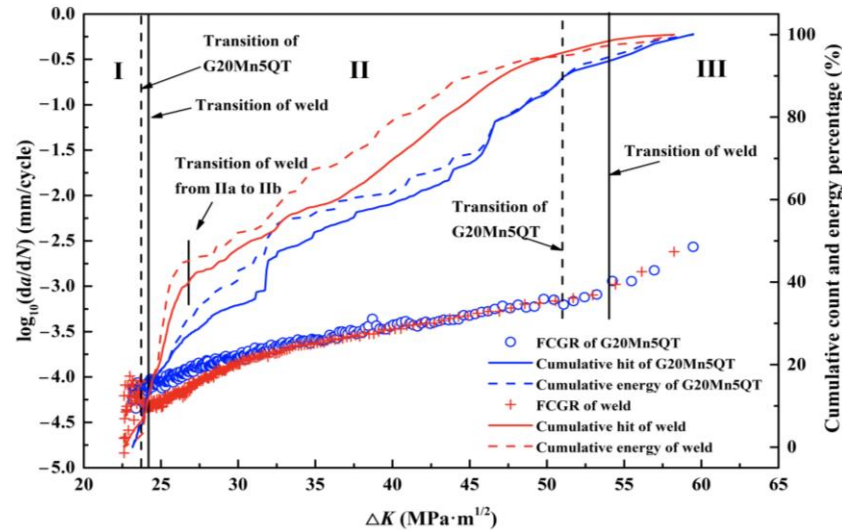

Figure 8. AE normalized cumulative hit and energy.

3.2. Cluster Analysis and Pattern Recognition

To conduct a detailed study of the AE source mechanisms, all the AE signals are classified into different types via the K-means cluster algorithm. The K-means is a cluster algorithm that partitions observations into k clusters, aiming to minimize the sum of Euclidean distances from signals to their clustering centroids. The K-means cluster algorithm has been proved to be efficient and reliable for AE signal analysis [43–45]. The value of k is artificially set. To obtain the optimum solution of k, the Davies and Bouldin (DB) index [46] is employed, and it can be expressed as in Equation (6):

$$DB = \frac{1}{c} \sum_{i=1, i \neq j}^{c} \max(\frac{d_i + d_j}{M_{ij}}),$$
(6)

where c is the number of clusters; d_i and d_j denote the average Euclidean distances of vectors in clusters i and j to the centroids of clusters i and j, respectively; and M_{ij} is the distance between the two clusters i and j. A lower value of the DB index indicates greater concentration in the cluster and separability between clusters.

To describe the AE signal, we employ five AE characteristics, comprising rise time, duration, ringing count, amplitude, and energy, to represent the waveform features of an AE signal. Some studies have indicated that these five characteristics demonstrate notable diversity against different damage patterns [43,47,48].

We simplify each AE signal to the above five characteristics and later introduce all the signals into the K-means cluster algorithm. The number of clusters is set from two to nine. Figure 9a shows the DB index values of for different cluster numbers. For both G20Mn5QT and the welds, the optimum cluster number is three. The proportions of the three clusters' AE signals are shown in Figure 9b. The proportion of cluster 1 is more than 70%, and that of cluster 2 is more than 20%. The proportion of cluster 3 is considerably lower than that of clusters 1 and 2.

To recognize the AE source pattern, the typical AE signals from each cluster for both G20Mn5QT and the weld are analyzed. The AE signals of cluster 1 are of a typical burst type, which has a short rise time and duration and a notable peak amplitude, which is

much stronger than that of other peaks (see Figure 10a,b). The AE signals of cluster 2 demonstrate a short rise time but a long duration. Unlike in the burst type, some strong peaks arise repeatedly after the peak amplitude (see Figure 10c,d). Therefore, cluster 2 can be confirmed to pertain to continuous-type signals. The research of Behnia et al. [49] indicated that burst-type AE signals in fatigue crack growth are released from metal fractures during tensile crack propagation, while continuous-type AE signals are released from the plastic deformation before the crack tip. When a tensile crack fracture occurs, the materials adjacent to the new crack separate, which leads to a transient volumetric change. The fracture generates a shear wave that consumes only a little energy and has a low propagation velocity and a longitudinal wave that consumes most of the energy and has a high propagation velocity. The two types of waves combine and create a wave with a .short rise time and duration. In addition, Ennaceur et al. [50] and Han et al. [51] suggested that continuous-type AE signals should be derived from the cyclic plastic deformation zone because the formation of stress–strain hysteresis loops occurs only in the cyclic plastic deformation zone. Vanniamparambil et al. [52] clarified the mechanism of the burst-type and continuous-type AE signals using another approach. They collected the AE signals before and after fatigue initiation using a CT specimen and noted that the AE signals before crack initiation were mainly of the continuous type, which can be released only from the cyclic plastic deformation of the material before the crack tip. Immediately after crack initiation, burst-type AE signals appeared, representing the fatigue crack propagation.
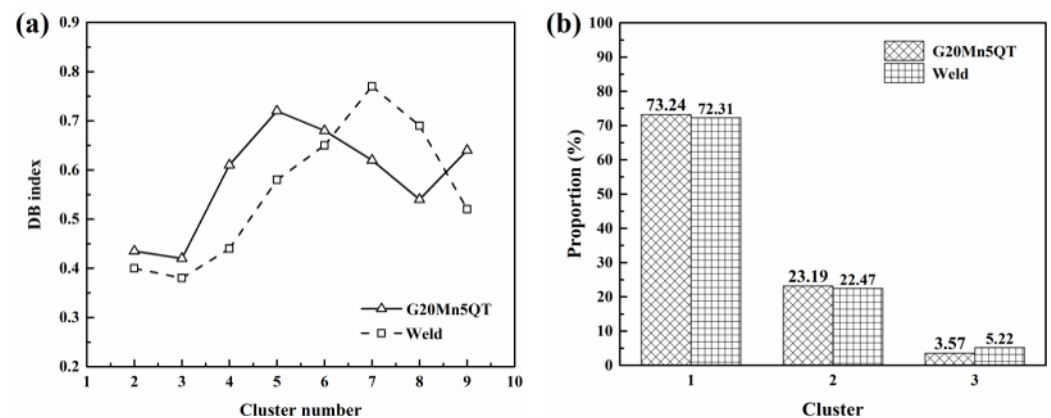

Figure 9. Cluster analysis of G20Mn5QT and weld: (**a**) DB index; (**b**) proportion of each cluster.

In addition, AE signals of cluster 3 are neither of the burst type nor the continuous type; these signals are similar to burst-type signals, albeit with a longer rise time and duration. The associated mechanism may be the shear crack fracture, which generates a shear wave that consumes most of the energy but has a low propagation velocity and a longitudinal wave that consumes less energy but has a high propagation velocity. The longitudinal wave and shear wave arrive at the AE sensor successively and then combine to form a combination-type signal that is similar to a burst type signal but has a relatively longer rise time and duration (see Figure 10e,f). This type of AE signal has been found previously In the studies of Chai [39] and Aggelis [53] and has been attributed to shear cracks. In other types of steel (316LN [39] and 304L [54]), these three types of AE waveform characteristics can also be observed.

To validate that the signals in cluster 3 are generated by shear crack fractures, the correlation between the RA and AF parameters is used. These two parameters are defined in Equations (7) and (8). RA is the ratio of rise time to peak amplitude and is measured in µs/v. AF is the ratio of ringing count to duration and is measured in kHz. The AE signal, due to the shear crack fracture, has a high RA and a low AF; while the AE signal, due to the tensile crack fracture, has a low RA and a high AF [53,55]. It can be found that cluster 3 signals distribute widely along the RA and have a small distribution range along the AF

(see Figure 11), while cluster 1 signals are the opposites of cluster 3 signals. Therefore, it can be reliably concluded that the mechanism of cluster 3 signals is related to shear crack fractures:

$$RA = \text{Rise time/Peak amplitude,} \tag{7}$$

$$AF = \text{Ringing count/Duration.} \tag{8}$$

Overall, cluster 1 is associated with tensile crack fractures, with the most AE signals; cluster 2 is associated with cyclic plastic deformations before the crack tip, with the second most AE signals; and cluster 3 is associated with shear crack fractures, with the fewest AE signals.
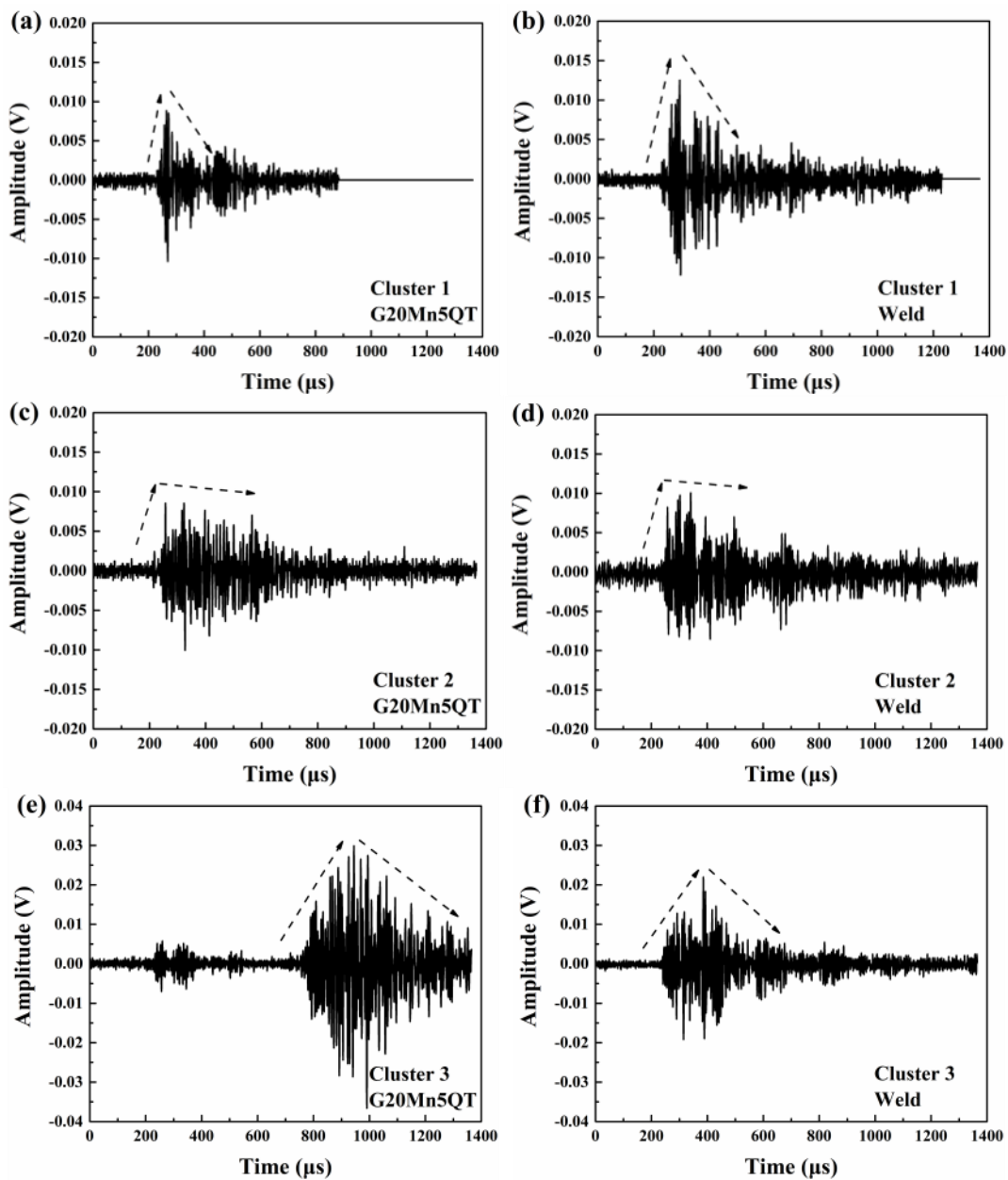

Figure 10. Waveforms of typical AE signals in different clusters: (**a**) cluster 1 signals of G20Mn5QT; (**b**) cluster 1 signals of welds; (**c**) cluster 2 signals of G20Mn5QT; (**d**) cluster 2 signals of welds; (**e**) cluster 3 signals of G20Mn5QT; (**f**) cluster 3 signals of welds.

The typical signal of each cluster is converted to the frequency spectrum by incorporating fast Fourier transform (see Figure 12). Similar to the research of Chang et al. [56], the frequency spectra of fatigue crack growth have three peaks. The frequencies of peaks 1, 2, and 3 are approximately 80 kHz, 150 kHz, and 280 kHz, respectively. Peak 2 has the largest magnitude, while the frequency of peak 1 exhibits a dense band composed of several peaks and has the second-largest magnitude. The dissimilarities between the frequency spectra of different clusters are not notable. For cluster 1, location 3 also exhibits a dense band, as does location 1; however, the magnitude is not excessively high. For clusters 2 and 3, location 3 has a significant peak in the dense band. Although the methodology of this research is based on experimental samples, the analysis method can also be applied to the potential practical implications of monitoring engineering structures.
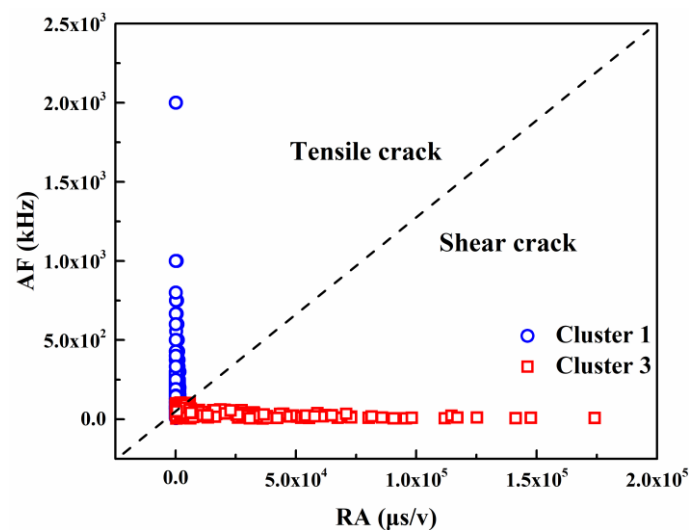

Figure 11. Correlation plot between RA and AF.

3.3. AE Behaviors and Fatigue Crack Growth Mechanism

After confirming that cluster 1 is related to tensile crack fractures, cluster 2 is related to cyclic plastic deformations, and cluster 3 is related to shear crack fractures, the behaviors of each cluster are analyzed to clarify the mechanism of fatigue crack growth further for both G20Mn5QT cast steel and related butt welds.

The dissimilarities in the AE signals among different clusters are reflected mainly in terms of the parameters of rise time, duration, and ringing count (see Figure 13). It can be noted that these three parameters increase with the increase in the cluster number. Therefore, AE signals released from shear crack fractures exhibit the largest rise time, duration, and ringing count; AE signals released from cyclic plastic deformations have the second-largest rise time, duration, and ringing count; and the AE signals released from tensile crack fractures have the smallest rise time, duration, and ringing count. Moreover, the corresponding three characteristics for the weld are larger than those pertaining to G20Mn5QT. This phenomenon has also been noted for metal 316 LN [39]. Generally, an AE signal with a larger rise time, duration, and ringing count carries a larger amount of energy. Therefore, shear crack fractures have the maximum average energy carried by an AE signal, cyclic plastic deformations have the second-largest average energy carried by an AE signal, and tensile crack fractures have the least average energy carried by an AE signal.
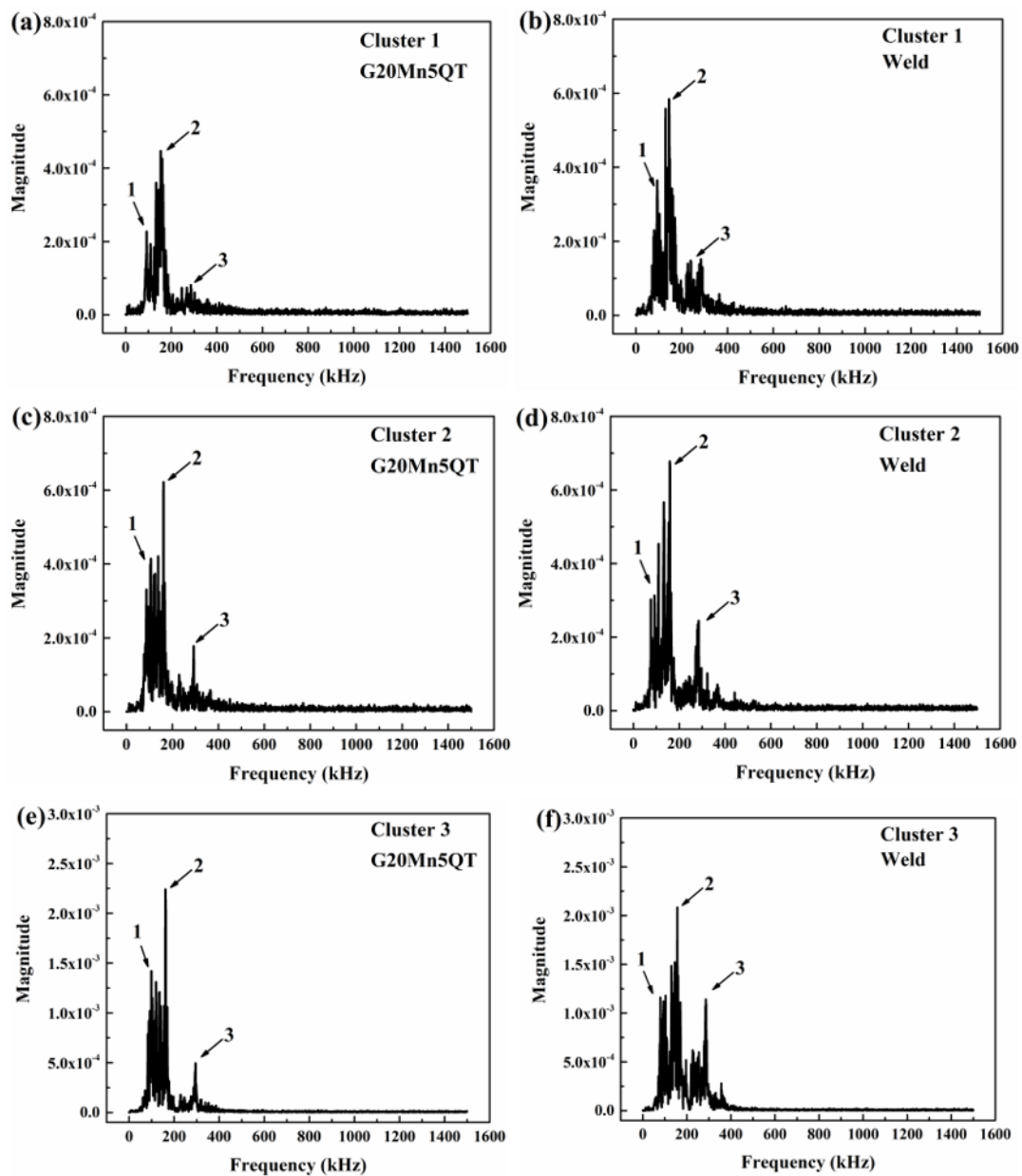
Figure 12. Frequency spectra of typical AE signals in different clusters: (**a**) cluster 1 signals of G20Mn5QT; (**b**) cluster 1 signals of welds; (**c**) cluster 2 signals of G20Mn5QT; (**d**) cluster 2 signals of welds; (**e**) cluster 3 signals of G20Mn5QT; (**f**) cluster 3 signals of welds.
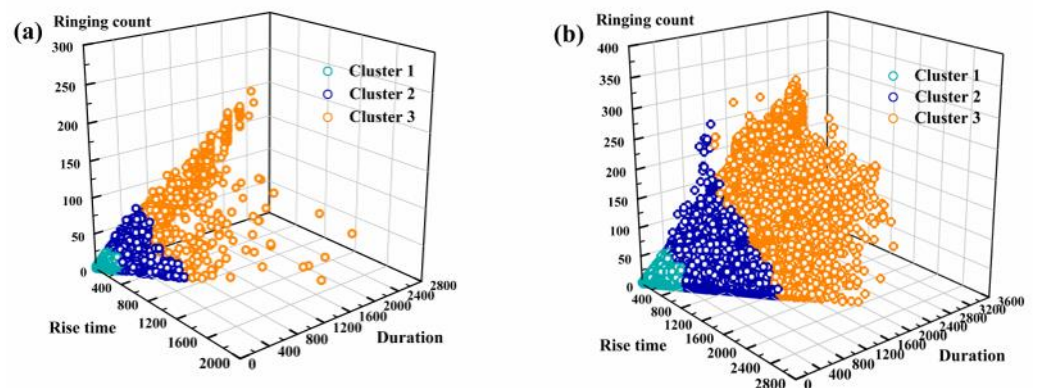

Figure 13. Wave characteristics for each cluster: (**a**) G20Mn5QT; (**b**) weld.

Figures 14 and 15 show the cumulative hit and energy of each cluster for both G20Mn5QT and welds. In Figures 14 and 15, the X-axis denotes the stress intensity factor range, and the Y-direction indicates the percentage of each cluster for all signals at the end of the experiment.
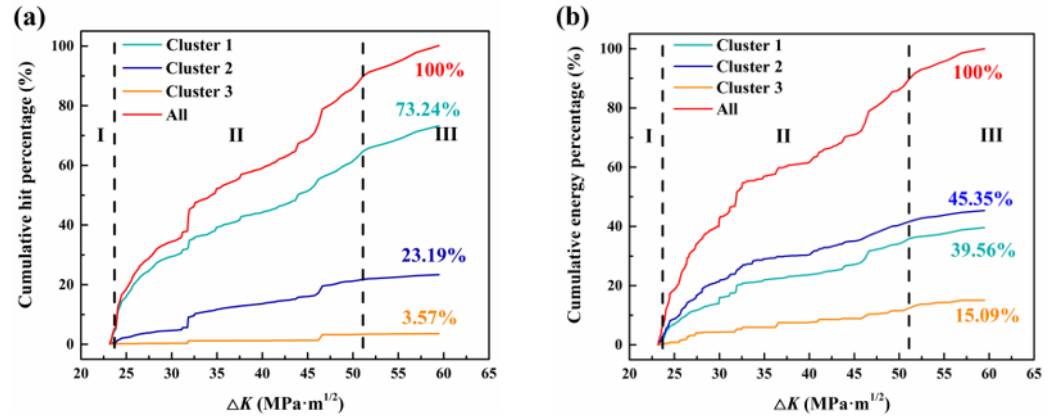

Figure 14. Cumulative AE of different clusters for G20Mn5QT: (**a**) hit; (**b**) energy.
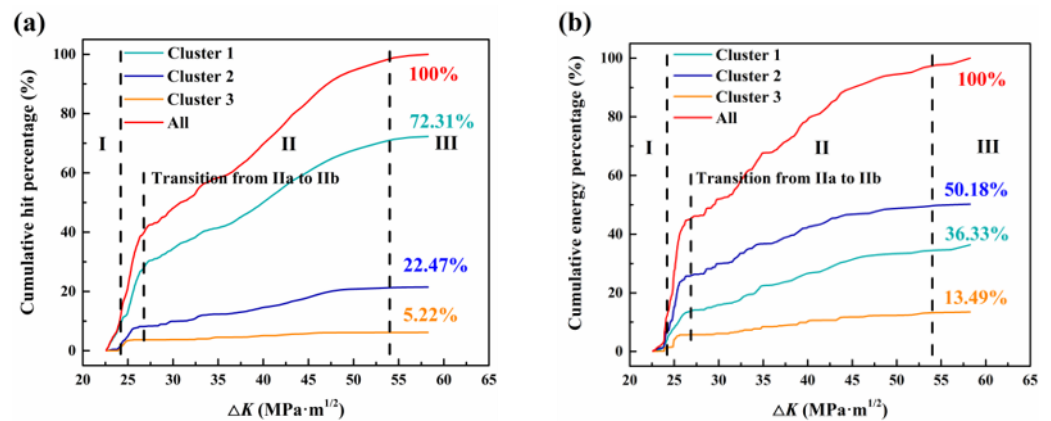

Figure 15. Cumulative AE of different clusters for the weld: (**a**) hit; (**b**) energy.

For G20Mn5QT cast steel, the increase in the AE hit is primarily due to the tensile crack fractures, whose contribution is much greater than that of clusters 2 and 3. However, cluster 2 has the largest contribution with regard to the increase in AE energy, and the corresponding contribution of cluster 1 is the second largest, being only slightly less than that of cluster 2. At the end of the test, clusters 1, 2, and 3 are noted to contribute 73.24%, 23.19%, and 3.57% to the cumulative hit and 39.56%, 45.35%, and 15.09% to the cumulative energy, respectively, as shown in Figure 14. At fatigue stage I and the beginning of stage II, both the hit and energy exhibit a fast growth rate.

For the weld, in trends similar to those for the G20Mn5QT, cluster 1 contributes the maximum to the hit, and its contribution to the energy is the second-largest; the contribution of cluster 2 to the hit is the second largest, and it contributes the largest in terms of energy; the contribution of cluster 3 to AE activity is small. At the end of the test, clusters 1, 2, and 3 are noted to contribute 72.31%, 22.47%, and 5.22% to the cumulative hit and 36.33%, 50.18%, and 13.49% to the cumulative energy, respectively. Unlike for G20Mn5QT cast steel, for the weld, the hit and energy growth rates generated by clusters 1 and 2 exhibit a transition point at the boundary between the two sub-stages in stage II, which is similar to the trend exhibited by the total cumulative hit and energy. However, cluster 3 does not demonstrate such a transition point. The cumulative hits for G20Mn5QT and the weld exhibit minor differences. However, the cumulative energy generated by cluster 2 of the weld is larger than that generated by cluster 2 of G20Mn5QT. On the contrary, the

cumulative energy values generated by clusters 1 and 3 of the weld are slightly less than those generated by clusters 1 and 3 of G20Mn5QT.

Based on the analysis discussed previously, fatigue crack growth is a combination of cyclic plastic deformation, tensile crack fractures, and shear crack fractures. Generally, AE signals pertain to stress waves released by deformations or crack fractures, and the signals' energies detected by the AE sensors are positively associated with the energies released by the deformations or fractures [57]. Cyclic plastic deformations before the crack tip release the maximum amount of energy, which is basically equal to the sum of the energies released by the tensile crack fractures and shear crack fractures. However, tensile crack fractures have the maximum number of occurrences, and this number is considerably larger than those for the others.

Furthermore, fatigue crack propagation can be regarded as a discontinuous crack tip advancement caused by fatigue damage accumulation before the crack tip, which has also been observed in an annealed, commercially pure iron (JIS-C2504) [58]. Fatigue damage before the crack tip—including slips, dislocations, fractures between crystals bonds, and so on—is caused by cyclic plastic deformations. Fatigue damage before the crack tip is the main factor leading to the further advancement of the crack front. The fatigue damage accumulation process releases around half of the total energy. When fatigue damage reaches critical status, the critical area of the material along the crack growth distance cannot bear the stress and ruptures in a brittle manner owing to a large number of tensile crack fractures and a small number of shear crack fractures; then, the crack tip advances a distance. The energy released by a single tensile crack fracture is quite small, but a large number of tensile crack fractures make the total accumulated energy slightly less than the energy released by the fatigue damage. The energy released by a single shear crack fracture is larger than that released by a single tensile crack fracture, but the total accumulated energy is the least. Moreover, it is worth noting that shear crack fractures are rarely observed in fatigue crack growth tests with CT specimens. Shear crack fractures appear as a discontinuity in acoustic emission signals, and a large amount of energy is carried by each signal. The mechanism of shear crack fractures is introduced in the next section.

3.4. Fractography Investigation

The fatigue fracture morphologies of the G20Mn5QT cast steel and the weld, after they were corroded using 5% alcohol nitrate solution, were observed using an S-3400N scanning electron microscope at the School of Material Science and Engineering, Tianjin University. Compared to that of G20Mn5QT, the crack surface of the butt weld is relatively flatter and smoother, and the necking zone of the butt weld appears much later (see Figure 16a,b). In stage I, the micromorphologies of both G20Mn5QT and the butt weld exhibit flat facets and fine fatigue striations with little secondary cracks, as shown in Figure 16c,d. As the fatigue crack propagates into stage II, the spacing of fatigue striations becomes wider and extremely evident. At the same time, secondary cracks appear extensively, as shown in Figure 16e,f. When the crack grows into stage III, dimples, tearing ridges, and secondary cracks begin to appear extensively. At the end of the cracks, ductile overload fracture morphologies characterized by microvoids and microcracks are predominant in the crack surfaces, as shown in Figure 16g,h.

It is worth noting that shear bands are observed on the fracture surfaces of G20Mn5QT and the butt weld. Furthermore, the shear bands are not continuously distributed along the surface but occur probabilistically around defects caused by casting or welding, as shown in Figure 17a,b. Therefore, the shear cracks appearing in the fracture surface of a CT specimen that should primarily exhibit tensile cracks may be caused by the multi-state of stress and strain occurring due to the casting or welding defects. This phenomenon verifies the existence of cluster 3 signals generated by shear crack fractures and the discontinuous occurrences pertaining to the discontinuous distributions of defects. Furthermore, as the average energy released by a shear crack fracture of G20Mn5QT

is less than that of the weld, the material weakening caused by the defects of G20Mn5QT is larger than that of the weld.
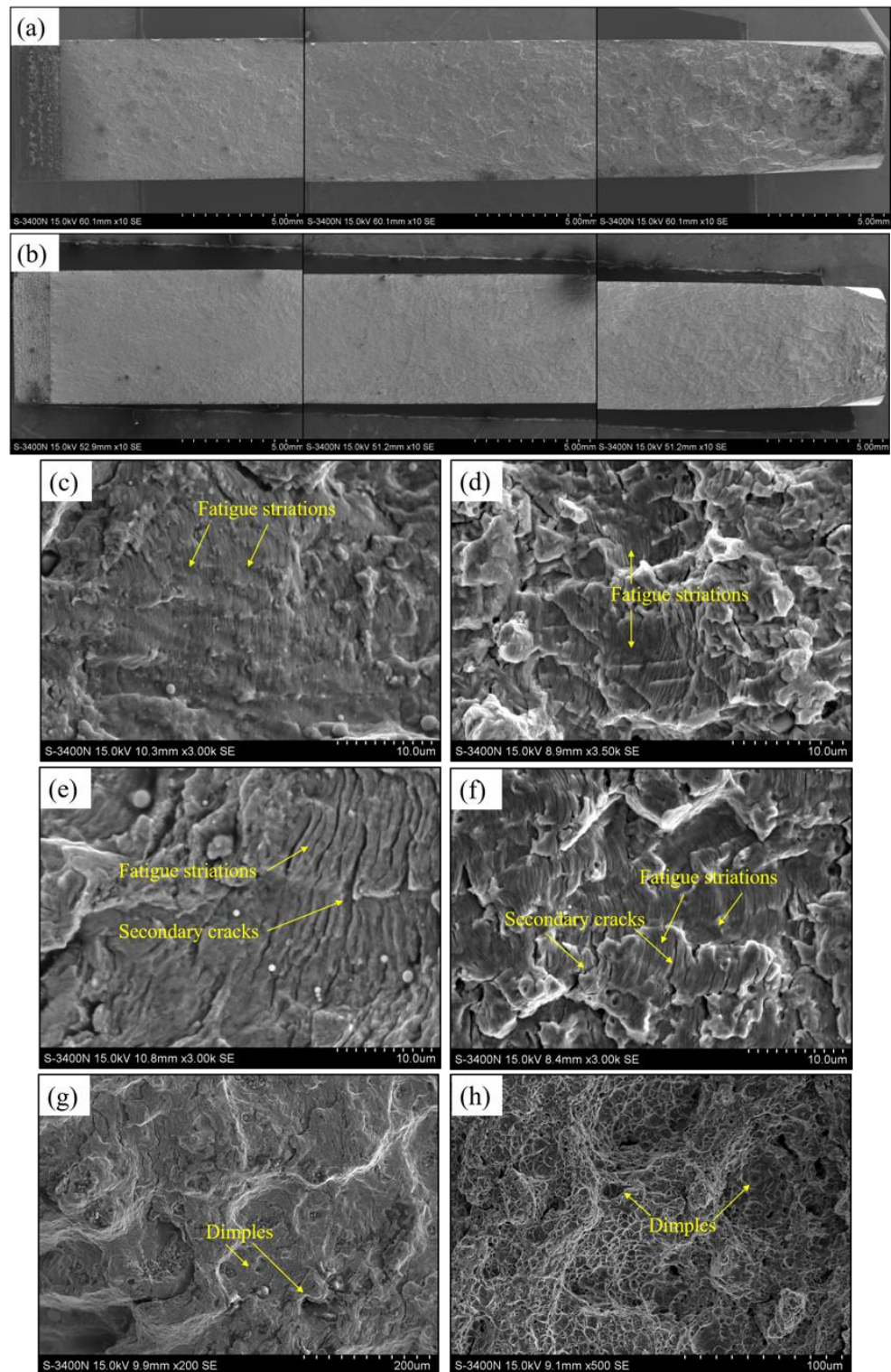
Figure 16. Scanning electron micrographs of crack surfaces: (**a**,**c**,**e**,**g**) G20Mn5QT cast steel; (**b**,**d**,**f**,**h**) butt weld; (**a**,**b**) crack surface; (**c**,**d**) fatigue striations at stage I; (**e**,**f**) fatigue striations at stage II; (**g**,**h**) dimples at stage III.
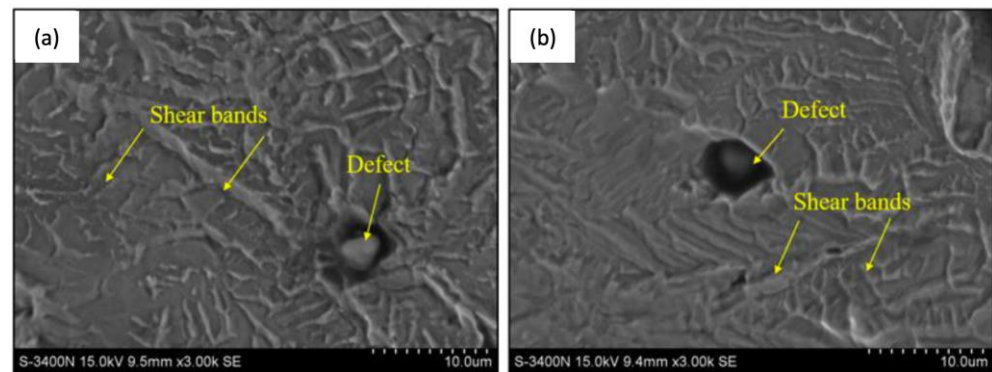
Figure 17. Scanning electron micrographs of crack surfaces: (**a**) shear bands of G20Mn5QT cast steel; (**b**) shear bands of butt weld.

4. Conclusions

In this research, fatigue crack growth experiments for G20Mn5QT and related butt welds were performed using CT specimens, and the corresponding AE signals were collected. By comparing and analyzing the AE behaviors, the following conclusions could be obtained:

(1) The AE activities vary greatly in different fatigue crack growth stages. The AE release activity of G20Mn5QT and butt welds reaches a peak at the end of fatigue crack stage I and decreases subsequently, demonstrating a relatively low level in the first half of stage II. The AE release activity returns to an increasing trend in the middle of stage II. The regrowth point for G20Mn5QT occurs earlier than that for the weld. Moreover, stage II of the welds can be further divided into two sub-stages based on the AE activity; however, G20Mn5QT does not exhibit such behavior.

(2) By introducing the K-means cluster algorithm, the AE signals for both G20Mn5QT and the weld can be divided into three clusters: cluster 1 pertains to the burst type with a short rise time and duration and is related to tensile crack fractures during fatigue crack growth; cluster 2 pertains to the continuous type with a short rise time and longer duration and is related to cyclic plastic deformations before the crack tip; and cluster 3 signals are similar to the burst type albeit with a long rise time and duration, and they are related to shear cracks.

(3) Fatigue crack growth is a combination of cyclic plastic deformations before the crack tip, tensile crack fractures, and shear crack fractures. Crack tip advancement can be regarded as the discontinuous process of the critical area brittlely rupturing as a large number of tensile crack fractures and rare shear crack fractures with fatigue damage due to cyclic plastic deformation reach critical status. The fatigue damage accumulation process releases around half of the total energy. The energy released by a single tensile crack fracture is quite small, but a large number of tensile crack fractures make the total accumulated energy slightly less than the energy released by fatigue damage. The energy released by a single shear crack fracture is larger than that released by a single tensile crack fracture, but the total accumulated energy is the least.

(4) Shear crack fractures in fatigue crack growth are induced by local multi-states of stress and strain caused by casting or welding defects. Shear crack fractures demonstrate discontinuous occurrences and pertain to the release of large average energies. The material weakening caused by the defects of G20Mn5QT is greater than that caused by the defects of the weld.

Author Contributions: Conceptualization, Q.L. and Z.Z.; methodology, G.L.; software, Y.X.; formal analysis, Q.L.; writing—original draft preparation, Y.X.; writing—review and editing, Q.L., J.X., and G.L.; supervision, G.L.; funding acquisition, J.X. All authors have read and agreed to the published version of the manuscript.

Institutional Review Board Statement: Not applicable.

Informed Consent Statement: Not applicable.

Data Availability Statement: The data presented in this study are available on request from the corresponding author due to privacy.

Conflicts of Interest: Authors Qingyang Liu and Zhenli Zhang was employed by the company Shandong Electric Power Engineering Consulting Institute Corp., Ltd. The remaining authors declare that the re-search was conducted in the absence of any commercial or financial relationships that could be construed as a potential conflict of interest.

References

1. *DIN EN 10293*; Steel Castings for General Engineering Steel Castings for General Engineering Uses. European Committee for Standardization (CEN): Brussels, Belgium, 2005.
2. Albiez, M.; Vallée, T.; Fricke, H.; Ummenhofer, T. Adhesively bonded steel tubes—Part I: Experimental investigations. *Int. J. Adhes. Adhes.* **2018**, *90*, 199–210. https://doi.org/10.1016/j.ijadhadh.2018.02.005.
3. Wei, Z.; Jin, H.; Chen, G. Traction structural stress analysis of fatigue behaviors of girth butt weld within welded cast steel joints. *Int. J. Press. Vessel. Pip.* **2020**, *179*, 104027. https://doi.org/10.1016/j.ijpvp.2019.104027.
4. Huang, S.; Shang, C.; Cai, L.; Wang, Z.; Hao, X. Effects of Cooling Procedures on Postfire Mechanical Properties and Fracture Resistance of G20Mn5QT Cast Steel. *J. Mater. Civ. Eng.* **2023**, *35*, 04023243. https://doi.org/10.1061/jmceet.mteng-15485.
5. Yin, Y.; Zhang, Y.; Lu, Y.; Xu, L.; Xin, J. Cyclic constitutive models for G20Mn5QT cast steel at low temperatures. *J. Constr. Steel Res.* **2022**, *193*, 107260. https://doi.org/10.1016/j.jcsr.2022.107260.
6. Xu, J.; Sun, T.; Xu Y，Han, Q. Fracture toughness research of G20Mn5QT cast steel based on the acoustic emission technique. *Constr. Build. Mater.* **2020**, *230*, 116904. https://doi.org/10.1016/j.conbuildmat.2019.116904.
7. Xu, Y.; Li, Z.; Xu, J.; Han, Q. Fatigue crack growth of G20Mn5QT cast steel based on a two-parameter driving force model. *Eng. Fract. Mech.* **2019**, *208*, 13–26. https://doi.org/10.1016/j.engfracmech.2018.12.028.
8. Han, Q.; Guo, Q.; Yin, Y.; Xing, Y. Fatigue behaviour of G20Mn5QT cast steel and butt welds with Q345B steel. *Int. J. Steel Struct.* **2016**, *16*, 139–149. https://doi.org/10.1007/s13296-016-3020-1.
9. Xu, J.; Sun Tong Sun Wen Xiao Wang, W.; Liu, X. J-R curve determination of G20Mn5QT cast steel using CT specimen with varying in-plane and out-of-plane constraints based on Normalization Method and GTN model. *J. Mater. Res. Technol.* **2022**, *18*, 3502–3519. https://doi.org/10.1016/j.jmrt.2022.04.006.
10. Lu, Y.; Wang, R.; Han, Q.; Yu, X.; Yu, Z. Experimental investigation on the corrosion and corrosion fatigue behavior of butt weld with G20Mn5QT cast steel and Q355D steel under dry–wet cycle. *Eng. Fail. Anal.* **2022**, *134*, 105977. https://doi.org/10.1016/j.engfailanal.2021.105977.
11. Han, Q.; Wang, Y.; Yin, Y.; Zhang, S. Fatigue tests on notched specimens of G20Mn5QT cast steel and life prediction by a new strain-based method. *Arch. Civ. Mech. Eng.* **2020**, *20*, 13. https://doi.org/10.1007/s43452-020-00114-1.
12. Eaton, M.J.; Crivelli, D.; Williams, R.; Byrne, C. Monitoring the drilling process of carbon fibre laminates using acoustic emission. *Proc. Inst. Mech. Eng. Part B J. Eng. Manuf.* **2023**, *237*, 1182–1193. https://doi.org/10.1177/09544054221124474.
13. Liu, S.; Qiao, S.; Xu, L.; Zhang, S.Z.; Ma, L.H.; Zhou, W. Acoustic emission monitoring and damage evaluation of bi-adhesive joint patch-repaired composites. *J. Adhes. Sci. Technol.* **2023**, *37*, 2461–2483. https://doi.org/10.1080/01694243.2022.2141500.
14. Seyyednourani, M.; Akgun, S.; Ulus, H.; Yildiz, M.; Sas, H.S. Experimental investigation on Compression-After-Impact (CAI) response of aerospace grade thermoset composites under low-temperature conditions assisted with acoustic emission monitoring. *Compos. Struct.* **2023**, *321*, 117260. https://doi.org/10.1016/j.compstruct.2023.117260.
15. Gagar, D.; Foote, P.; Irving, P.E. Effects of loading and sample geometry on acoustic emission generation during fatigue crack growth: Implications for structural health monitoring. *Int. J. Fatigue* **2015**, *81*, 117–127. https://doi.org/10.1016/j.ijfatigue.2015.07.024.
16. Shi, S.; Wu, G.; Chen, H.; Zhang, S. Acoustic Emission Monitoring of Fatigue Crack Growth in Hadfield Steel. *Sensors* **2023**, *23*, 6561. https://doi.org/10.3390/s23146561.
17. Han, Z.; Luo, H.; Cao, J.; Wang, H. Acoustic emission during fatigue crack propagation in a micro-alloyed steel and welds. *Mater. Sci. Eng. A* **2011**, *528*, 7751–7756. https://doi.org/10.1016/j.msea.2011.06.065.
18. Kumar, J.; Ahmad, S.; Mukhopadhyay, C.K.; Jayakumar, T.; Kumar, V. Acoustic emission studies for characterization of fatigue crack growth behavior in HSLA steel. *Nondestruct. Test. Eval.* **2016**, *31*, 77–96. https://doi.org/10.1080/10589759.2015.1070850.
19. Moorthy, V.; Jayakumar, T.; Raj, B. Influence of micro structure on acoustic emission behavior during stage 2 fatigue crack growth in solution annealed, thermally aged and weld specimens of AISI type 316 stainless steel. *Mater. Sci. Eng. A* **1996**, *212*, 273–280. https://doi.org/10.1016/0921-5093(0206-9.
20. Shen, G.; Shen, Y.; Yuan, Y. Study of the acoustic emission characteristics of weld cracks in carbon steel pressure vessels. *Insight-Non-Destr. Test. Cond. Monit.* **2022**, *64*, 496–502. https://doi.org/10.1784/insi.2022.64.9.496.

21. Barat, V.; Marchenkov, A.; Bardakov, V.; Zhgut, D.; Karpova, M.; Balandin, T.; Elizarov, S. Assessment of the structural state of dissimilar welded joints by the acoustic emission method. *Appl. Sci.* **2022**, *12*, 7213. https://doi.org/10.3390/app12147213.

22. Carrion-Viramontes, F.J.; Hernandez-Figueroa, J.A.; Machorro-Lopez, J.M.; Quintana-Rodriguez, J.A. Weld acoustic emission inspection of structural elements embedded in concrete. *Sci. Prog.* **2022**, *105*, 368504221075482. https://doi.org/10.1177/00368504221075482.

23. Xu, J.; Wang, K.; Ma, Q.; Li, H.; Wang, P.; Chen, R.; Wang, P.; Chen, R.; Qian, Y.; Zeng, D. Study on acoustic emission properties and crack growth rate identification of rail steels under different fatigue loading conditions. *Int. J. Fatigue* **2023**, *172*, 107638. https://doi.org/10.1016/j.ijfatigue.2023.107638.

24. Chai, M.; Lai, C.; Xu, W.; Duan, Q.; Zhang, Z.; Song, Y. Characterization of fatigue crack growth based on acoustic emission multi-parameter analysis. *Materials* **2022**, *15*, 6665. https://doi.org/10.3390/ma15196665.

25. Ren, H.; An, G.; Hao, L.; Wand, Z. Experimental Study on PLC Effect and Acoustic Emission Characteristics of Aluminum Alloy. *Trans. Beijing Inst. Technol.* **2019**, *39*, 999–1005. DOI: 10.15918/j.tbit1001-0645.2019.10.002.

26. Younis, H.B.; Kamal, K.; Sheikh, M.F.; Hamza, A. Prediction of fatigue crack growth rate in aircraft aluminum alloys using optimized neural networks. *Theor. Appl. Fract. Mech.* **2022**, *117*, 103196. https://doi.org/10.1016/j.tafmec.2021.103196.

27. Baptista, R.; Moita, P.; Infante, V. Fatigue crack growth on modified CT specimens using artificial neural networks. *Int. J. Fatigue* **2023**, *167*, 107357. https://doi.org/10.1016/j.ijfatigue.2022.107357.

28. Megid, W.A.; Chainey, M.; Lebrun, P.; Robert Hay, D. Monitoring fatigue cracks on eyebars of steel bridges using acoustic emission: A case study. *Eng. Fract. Mech.* **2019**, *211*, 198–208. https://doi.org/10.1016/j.engfracmech.2019.02.022.

29. Megid, W.A.; Mejia, J.; Modwel, R.; Hay, D.R. Monitoring Welded Joints of Steel Pressure Vessels Using Acoustic Emission: Case Study. *Trans. Indian Inst. Met.* **2022**, *75*, 2199–2209. https://doi.org/10.1007/s12666-022-02599-1.

30. Rivera, F.G.; Edwards, G.; Eren, E.; Soua, S. Acoustic emission technique to monitor crack growth in a mooring chain. *Appl. Acoust.* **2018**, *139*, 156–164. https://doi.org/10.1016/j.apacoust.2018.04.034.

31. Manuello Bertetto, A.; Masera, D.; Carpinteri, A. Acoustic emission monitoring of the turin cathedral bell tower: Foreshock and aftershock discrimination. *Appl. Sci.* **2020**, *10*, 3931. https://doi.org/10.3390/app10113931.

32. Kundu, T.; Datta, A.K.; Topdar, P.; Sengupta, S. Optimal location of acoustic emission sensors for detecting rail damage. *Proc. Inst. Civ. Eng.-Struct. Build.* **2022**, *177*, 254–263. https://doi.org/10.1680/jstbu.21.00074.

33. Iziumova, A.Y.; Vshivkov, A.N.; Prokhorov, A.E.; Panteleev, I.A.; Mubassarova, V.A.; Plekhov, O.A.; Linderov, M.L.; Merson, D.L.; Vinogradov, A. Heat dissipation and acoustic emission features of titanium alloys in cyclic deformation mode. *Acta Mech.* **2021**, *232*, 1853–1861. https://doi.org/10.1007/s00707-020-02911-4.

34. Liu, M.; Lu, J.; Lou, B. Research on Kaiser effect of acoustic emission in concrete subjected to bending after freeze-thaw. *J. Build. Eng.* **2023**, *78*, 107713. https://doi.org/10.1016/j.jobe.2023.107713.

35. Saeedifar, M.; Zarouchas, D. Damage characterization of laminated composites using acoustic emission: A review. *Compos. Part B Eng.* **2020**, *195*, 108039. https://doi.org/10.1016/j.compositesb.2020.108039.

36. Zhou, Y.; Li, L.; Liu, Y.; Zhang, Z.; Matsui, T. Clustering analysis of acoustic emission signals in the monitoring of stone monuments: Case of the freeze–thaw deterioration of tuffs. *Herit. Sci.* **2023**, *11*, 1–20. https://doi.org/10.1186/s40494-023-00962-z.

37. Sause, M.G.R.; Gribov, A.; Unwin, A.R.; Horn, S. Pattern recognition approach to identify natural clusters of acoustic emission signals. *Pattern Recognit. Lett.* **2012**, *33*, 17–23. https://doi.org/10.1016/j.patrec.2011.09.018.

38. Pascoe, J.A.; Zarouchas, D.S.; Alderliesten, R.C.; Benedictus, R. Using acoustic emission to understand fatigue crack growth within a single load cycle. *Eng. Fract. Mech.* **2018**, *194*, 281–300. https://doi.org/10.1016/j.engfracmech.2018.03.012.

39. Chai, M.; Zhang, J.; Zhang, Z.; Duan, Q.; Cheng, G. Acoustic emission studies for characterization of fatigue crack growth in 316LN stainless steel and welds. *Appl. Acoust.* **2017**, *126*, 101–113. https://doi.org/10.1016/j.apacoust.2017.05.014.

40. *ASTM Standard E647*; Standard Test Method for Measurement of Fatigue Crack Growth Rates. ASTM International: West Conshohocken, PA, USA, 2004.

41. Mostafapour, A.; Ghareaghaji, M.; Davoodi, S.; Ebrahimpour, A. Theoretical analysis of plate vibration due to acoustic signals. *Appl. Acoust.* **2016**, *103*, 82–89. https://doi.org/10.1016/j.apacoust.2015.09.018.

42. Paris, P.; Erdogan, F. A critical analyses of crack propagation laws. *J. Basic Eng.* **1963**, *85*, 528–533. https://doi.org/10.1115/1.3656900.

43. Han, Q.; Yang, G.; Xu, J.; Fu, Z.; Lacidogna, G.; Carpinteri, A. Acoustic emission data analyses based on crumb rubber concrete beam bending tests. *Eng. Fract. Mech.* **2019**, *210*, 189–202. https://doi.org/10.1016/j.engfracmech.2018.05.016.

44. Carvelli, V.; D'Ettorre, A.; Lomov, S.V. Acoustic emission and damage mode correlation in textile reinforced PPS composites. *Compos. Struct.* **2017**, *163*, 399–409. https://doi.org/10.1016/j.compstruct.2016.12.012.

45. Gutkin, R.; Green, C.J.; Vangrattanachai, S.; Pinho, S.T.; Robinson, P.; Curtis, P.T. On acoustic emission for failure investigation in CFRP: Pattern recognition and peak frequency analyses. *Mech. Syst. Signal Process.* **2011**, *25*, 1393–1407. https://doi.org/10.1016/j.ymssp.2010.11.014.

46. Davies, D.L.; Bouldin, D.W. A Cluster Separation Measure. *IEEE Trans. Pattern Anal. Mach. Intell.* **1979**, *PAMI-1*, 224–227. https://doi.org/10.1109/TPAMI.1979.4766909.

47. Nguyen-Tat, T.; Ranaivomanana, N.; Balayssac, J.P. Characterization of damage in concrete beams under bending with Acoustic Emission Technique (AET). *Constr. Build. Mater.* **2018**, *187*, 487–500. https://doi.org/10.1016/j.conbuildmat.2018.07.217.

48. Kozak, K.; Dosi, A.; Bućko, M.M.; Chlubny, L.; Lis, J.; Antou, G.; Chotard, T. Investigation of the mechanical behavior of MAX phases by acoustic emission technique. *Mater. Sci. Eng. A* **2017**, *707*, 73–80. https://doi.org/10.1016/j.msea.2017.09.030.

49. Behnia, A.; Chai, H.K.; GhasemiGol, M.; Sepehrinezhad, A.; Mousa, A.A. Advanced damage detection technique by integration of unsupervised clustering into acoustic emission. *Eng. Fract. Mech.* **2019**, *210*, 212–227. https://doi.org/10.1016/j.engfracmech.2018.07.005.

50. Ennaceur, C.; Laksimi, A.; Hervé, C.; Cherfaoui, M. Monitoring crack growth in pressure vessel steels by the acoustic emission technique and the method of potential difference. *Int. J. Press. Vessel. Pip.* **2006**, *83*, 197–204. https://doi.org/10.1016/j.ijpvp.2005.12.004.

51. Han, Z.; Luo, H.; Sun, C.; Li, J.; Papaelias, M.; Davis, C. Acoustic emission study of fatigue crack propagation in extruded AZ31 magnesium alloy. *Mater. Sci. Eng. A* **2014**, *597*, 270–278. https://doi.org/10.1016/j.msea.2013.12.083.

52. Vanniamparambil, P.A.; Guclu, U.; Kontsos, A. Identification of Crack Initiation in Aluminum Alloys using Acoustic Emission. *Exp. Mech.* **2015**, *55*, 837–850. https://doi.org/10.1007/s11340-015-9984-5.

53. Aggelis, D.G.; Kordatos, E.Z.; Matikas, T.E. Acoustic emission for fatigue damage characterization in metal plates. *Mech. Res. Commun.* **2011**, *38*, 106–110. https://doi.org/10.1016/j.mechrescom.2011.01.011.

54. Amer, A.O.; Gloanec, A.L.; Courtin, S.; Touze, C. Characterization of Fatigue Damage in 304L Steel by an Acoustic Emission Method. *Procedia Eng.* **2013**, *66*, 651–660. https://doi.org/10.1016/j.proeng.2013.12.117.

55. RILEM Technical Committee (Masayasu Ohtsu). Recommendation of RILEM TC 212-ACD: Acoustic emission and related NDE techniques for crack detection and damage evaluation in concrete*. *Mater. Struct.* **2010**, *43*, 1187–1189. https://doi.org/10.1617/s11527-010-9640-6.

56. Chang, H.; Han, E.; Wang, J.; Ke, W. Acoustic emission study of fatigue crack closure of physical short and long cracks for aluminum alloy LY12CZ. *Int. J. Fatigue* **2009**, *31*, 403–407. https://doi.org/10.1016/j.ijfatigue.2008.08.008.

57. Zárate, B.A.; Caicedo, J.M.; Yu, J.; Ziehl, P. Probabilistic Prognosis of Fatigue Crack Growth Using Acoustic Emission Data. *J. Constr. Steel Res.* **2012**, *138*, 1101–1111. https://doi.org/10.1016/j.jcsr.2012.03.002.

58. Birenis, D.; Ogawa, Y.; Matsunaga, H.; Takakuwa, O.; Yamabe, J.; Prytz, Ø.; Thøgersen, A. Hydrogen-assisted crack propagation in α-iron during elasto-plastic fracture toughness tests. *Mater. Sci. Eng. A* **2019**, *756*, 396–404. https://doi.org/10.1016/j.msea.2019.04.084.